

Spectroscopic Studies of Bridge Contributions to Electronic Coupling in a Donor-Bridge-Acceptor Biradical System

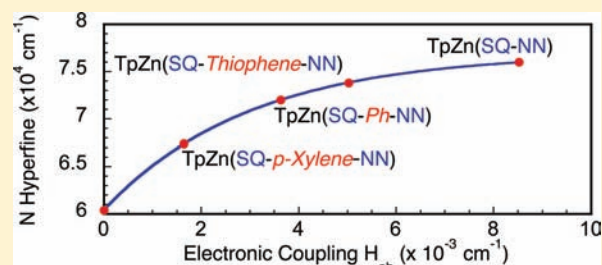
Martin L. Kirk,^{*,†} David A. Shultz,^{*,‡} Ezra C. Depperman,[†] Diana Habel-Rodriguez,[†] and Robert D. Schmidt[‡]

[†]Department of Chemistry and Chemical Biology, The University of New Mexico, MSC03 2060, 1 University of New Mexico, Albuquerque, New Mexico 87131-0001, United States

[‡]Department of Chemistry, North Carolina State University, Raleigh, North Carolina 27695-8204, United States

S Supporting Information

ABSTRACT: Variable-temperature electronic absorption and resonance Raman spectroscopies are used to probe the excited state electronic structure of $\text{Tp}^{\text{Cum,Me}}\text{Zn}(\text{SQ-Ph-NN})$ (1), a donor-bridge-acceptor (D-B-A) biradical complex and a ground state analogue of the charge-separated excited state formed in photo-induced electron transfer reactions. Strong electronic coupling mediated by the *p*-phenylene bridge stabilizes the triplet ground state of this molecule. Detailed spectroscopic and bonding calculations elucidate key bridge distortions that are involved in the $\text{SQ}(\pi)_{\text{SOMO}} \rightarrow \text{NN-Ph}(\pi^*)_{\text{LUMO}} \text{D} \rightarrow \text{A}$ charge transfer (CT) transition. We show that the primary excited state distortion that accompanies this CT is along a vibrational coordinate best described as a symmetric $\text{Ph}(8a) + \text{SQ}(\text{in-plane})$ linear combination and underscores the dominant role of the phenylene bridge fragment acting as an electron acceptor in the D-B-A charge transfer state. Our results show the importance of the phenylene bridge in promoting (1) electron transfer in D-Ph-A systems and (2) electron transport in biased electrode devices that employ a 1,4-phenylene linkage. We have also developed a relationship between the spin density on the acceptor, as measured via the isotropic NN nitrogen hyperfine interaction, and the strength of the $\text{D} \rightarrow \text{A}$ interaction given by the magnitude of the electronic coupling matrix element, H_{ab} .



INTRODUCTION

Considerable effort has been expended in developing an understanding of how molecular bridge (B) fragments facilitate electron transfer over long distances. The fundamental mechanisms responsible for nonresonant electron transfer processes in molecular systems¹ include superexchange, which involves electron (e^-) or hole (h^+) transfer via the bridge without discrete redox changes in the bridge, incoherent e^-/h^+ tunneling, and thermally activated hopping. The latter mechanism involves discrete oxidation or reduction of the bridge fragment. A number of models have been developed to understand adiabatic and nonadiabatic electron transfer rates as a function of thermodynamic driving force and the geometry and nature of the bridge in photoinduced electron transfer (PET) reactions between donor (D) and acceptor (A) fragments in a D-B-A system.^{2–17} In the PET process, photoexcitation of D yields a $\text{D}^*\text{-B-A}$ excited state that may undergo facile electron transfer to form a spin singlet biradical $\text{D}^+\text{-B-A}^-$ charge separated state. Photogenerated $\text{D}^+\text{-B-A}^-$ biradicals have been used to probe structural effects on electron transfer rates by correlating the magnetic exchange interaction, J , with the electronic coupling matrix element H_{ab} .^{1,16,18–21} These data show that ET rates through phenyl bridges possess exponential distance dependence with $\beta \approx 0.5$, in excellent agreement with theory and direct electron transfer

rate studies. Recently, we showed that covalently linked, non-disjoint heterospin triplet D-A biradicals (Figure 1) may be thought of as ground state analogues of the charge separated states that derive from PET. In these studies, a valence bond configuration interaction (VBCI) model that utilizes spectroscopic and magnetic observables was used to understand the electronic origin of both H_{ab} and the strong ferromagnetic coupling in the semiquinone nitronitroxide (SQ-NN) D-A biradical series, $\text{Tp}^{\text{Cum,Me}}\text{M}(\text{SQ-NN})$.²²

Electron transport mediated by single molecule bridges (wires) that span nanoscale electrodes ($\text{E}_{(\pm)}$) can be related to PET processes. In these $\text{E}_{(+)}\text{-molecule-E}_{(-)}$ systems, an applied nanoelectrode bias can result in electron transport across the molecular wire.^{23,24} Molecular electron transport systems have been devised to promote spin polarized electron transport by using magnetic electrodes and magnetic bridge fragments and to allow for unidirectional electron transport (molecular rectification) by asymmetric attachment of the bridge to the electrodes or by using an asymmetric D-A type bridge fragment.^{25–27} With respect to molecular rectification, Aviram and Ratner²⁸ originally suggested that a covalently linked D-B-A molecule could function as a molecular rectifier²⁶ and allow

Received: January 9, 2012

Published: April 5, 2012

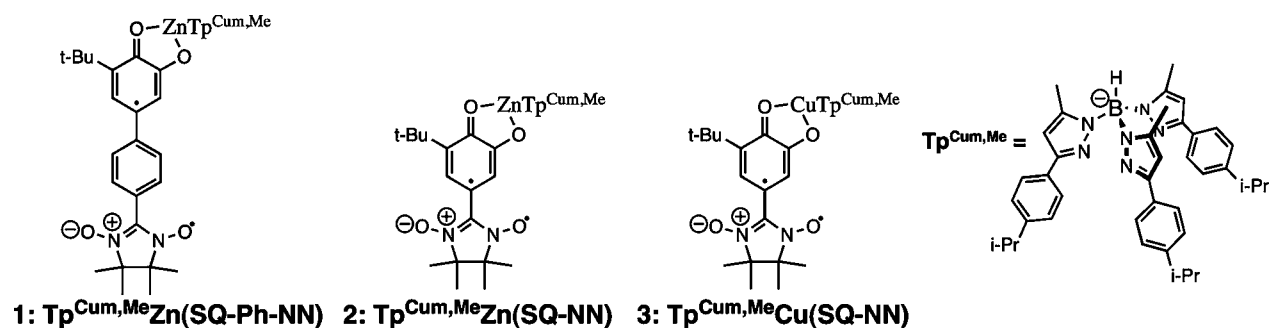


Figure 1. Donor-acceptor and donor-bridge-acceptor biradicals used in this study.

for unidirectional current flow via the formation of a $\text{D}^+\text{-B-A}^-$ electronic configuration at appropriate bias voltages. These rectifying $\text{D}^+\text{-B-A}^-$ bridges can be described as donor-acceptor biradicals that have been created by e^- or h^+ injection into the A or D fragments from the electrode Fermi levels. Thus, it is the inherent electronic asymmetry in a D-B-A system that may allow unidirectional electron transport. Both the magnitude of the D-B-A coupling, H_{ab} , and the inherent electronic structure of the bridge fragment are likely to provide key contributions to a high rectification ratio and a properly functioning rectifying device.

Key questions in molecular electron transfer/transport focus on (1) determining the magnitude of the electronic coupling mediated by a given molecular bridge fragment, (2) relating the magnitude of the electronic coupling to the intimate electronic and geometric structure of the bridge, and (3) understanding the nature of molecular distortions in the bridge that are coupled to electron transfer/transport. Understanding bridge contributions to D-B-A electron transfer/transport is particularly important in light of recent work which has shown that a molecular junction formed by a single benzene molecule bridging two biased Pt electrodes results in electron transport with a conductance approaching the maximum allowed for single channel conductance, G_0 .^{29,30} Prior studies by our group on $\text{Tp}^{\text{Cum,Me}}\text{Zn}(\text{SQ-bridge-NN})$ molecules focused on using EPR spectroscopy to understand the spin density distributions, bridge conformations, and the degree of $\text{D} \rightarrow \text{A}$ charge transfer in these biradicals.³¹ In this manuscript, we use a combination of variable temperature electronic absorption and resonance Raman spectroscopies to probe the nature of the bridge fragment in $\text{Tp}^{\text{Cum,Me}}\text{Zn}(\text{SQ-Ph-NN})$ **1**, which possesses a semiquinone radical (SQ) donor, a nitronyl nitroxide radical (NN) acceptor, and a phenylene bridge that constitute a D-B-A array. The spectroscopic studies have been evaluated in the context of detailed bonding calculations and, through the use of a valence bond configuration interaction (VBCI) model, allow for deep insight into how the excited state electronic structure and the nature of the bridge fragment affect the magnitude of H_{ab} mediated by a phenylene. Coupled with our earlier work,³¹ this has also allowed us to develop a relationship between experimentally determined H_{ab} values and isotropic nitrogen hyperfine parameters on the NN acceptor fragment.

EXPERIMENTAL SECTION

General Considerations. All compounds were synthesized as previously described.^{32,33}

Electronic Absorption Spectroscopy. Electronic absorption spectra were collected on a Hitachi U-3501 UV-vis-NIR spectrophotometer capable of scanning a wavelength region between 185 and 3200 nm using a double-beam configuration at 2.0 nm resolution.

The instrument wavelength was calibrated with reference to the 656.10 nm deuterium line. Background spectra were collected to correct for residual absorption due to the solvent and automatically subtracted from the sample spectrum by the Hitachi Grams software. Low temperature (~ 10 K) spectra were collected using a Janis STVP-100 continuous flow cryostat mounted in a custom designed cradle assembly, and the sample temperature was monitored with a Lakeshore silicon-diode (PT-470) and regulated by a combination of helium flow and dual heater assemblies. Solution spectra were collected in 1.0 mm path length spectroil quartz masked cells (Starna). Solution samples were prepared in dichloromethane or methylcyclohexane. Solid-solution spectra were collected on thin polystyrene (MW = 280,000) polymer films prepared by evaporation of the saturated polystyrene solutions dispersed on glass. Gaussian resolution of spectral bands and corrections for light scattering were accomplished with the Grams 386 software package.

Resonance Raman Spectroscopy. Coherent Innova 70-5 Ar^+ ion (457.9, 528.7 nm) and Coherent Innova 300C Kr^+ ion (406.7, 676.47 nm) lasers were used as the excitation sources. The scattered radiation was dispersed onto a liquid N_2 cooled 1" Spex Spectrum One CCD detector using a Spex 1877E triple grating monochromator equipped with 600, 1200, and 1800 gr/mm holographic gratings at the spectrographic stage. The laser power at the sample was kept between 40 and 100 mW to prevent thermal or photo degradation of the sample. Raman data were collected as dichloromethane solutions. The prepared sample was then sealed in an NMR tube with a rubber septum and Parafilm. Room temperature spectra were obtained with the sample tube placed in a modified NMR sample holder/spinner and collected using a 135° backscattering geometry.

Electronic Structure Calculations. Spin unrestricted gas-phase geometry optimizations for compounds **1** and **2** were performed at the density functional level of theory using the Gaussian 03W software package.³⁴ All calculations employed the B3LYP hybrid functional, and a 6-31G(d,p') basis set, a split valence basis set with polarizability functions, was used for all atoms. Input files were prepared using the molecule builder function in the Gaussview software package, and the *tert*-butyl substituent on the semiquinone was modeled as a methyl group. Frontier molecular orbitals (MOs) were generated for the optimized ground states. Frequency calculations were performed on the geometry optimized SQ-Ph-NN and SQ-NN ligands. Time-dependent DFT calculations were performed on the optimized ground-state geometries, and the first 20 excited states were calculated. Electron density difference maps (EDDMs) were constructed from the output of the time-dependent calculations using the GaussSum suite of programs.³⁵

RESULTS AND DISCUSSION

Frontier Molecular Orbitals, Electronic Absorption Spectroscopy, and Band Assignments. We present a simplified molecular orbital diagram showing the relevant SQ, Ph, and NN frontier molecular orbitals (MOs) of **1** in Figure 2. This simplified MO diagram was derived from the results of DFT and Hückel bonding calculations and is similar to the diagram we previously presented for **2**, which lacks a phenylene

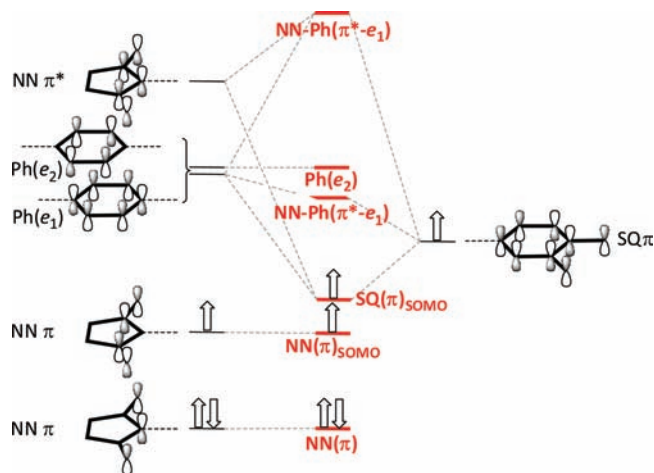


Figure 2. Qualitative π -molecular orbital diagram for **1**.

bridge.²² Here we have included the doubly degenerate, in the D_{6h} symmetry of the bridge, lowest unoccupied molecular orbital (LUMO) set localized on the Ph bridge ($\text{Ph}(e_1)$ and $\text{Ph}(e_2)$). The bonding calculations indicate strong orbital mixing between the $\text{NN}(\pi^*)$ and $\text{Ph}(e_1)$ orbitals leading to an energetically stabilized $\text{NN-Ph}(\pi^*-e_1)$ bonding MO. The $\text{Ph}(e_2)$ orbital does not possess the appropriate symmetry to interact with the SQ and NN frontier MOs and is essentially nonbonding in character. We have used the results of these bonding calculations, time-dependent density functional theory (TD-DFT) calculations, and previous spectral assignments for **2**, $\text{Tp}^{\text{Cum,Me}}\text{Cu}(\text{SQ-NN})$ (**3**), aryl-nitronyl nitroxide (Ar-NN), and other SQ-based chromophores to assign the prominent spectral features in **1**.²²

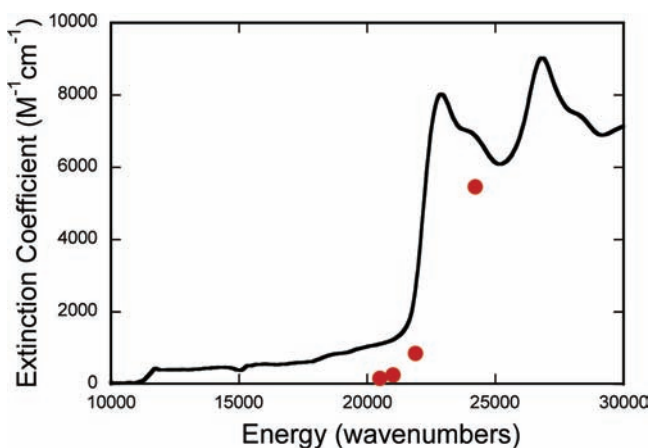


Figure 3. Room temperature solution electronic absorption spectrum of **1** and resonance Raman excitation profile of the 1591 cm^{-1} vibration showing large resonance enhancement of this mode when exciting into the $\text{SQ}(\pi)_{\text{SOMO}} \rightarrow \text{NN-Ph}(\pi^*-e_1)$ CT band (see text).

The room temperature solution electronic absorption spectrum of $\text{Tp}^{\text{Cum,Me}}\text{Zn}(\text{SQ-Ph-NN})$ (**1**) is presented in Figure 3. Numerous electronic transitions are observed between $\sim 11,000$ and $\sim 20,000\text{ cm}^{-1}$ in $\text{Tp}^{\text{Cum,Me}}\text{M}(\text{SQ-NN})$ compounds,^{22,36} all of which possess relatively weak intensity ($\epsilon \approx 400\text{--}1,100\text{ M}^{-1}\text{ cm}^{-1}$). The most intense of these transitions have been assigned as $\text{NN}(\pi) \rightarrow \text{SQ}(\pi)_{\text{SOMO}}$, $\text{SQ}(n) \rightarrow \text{SQ}(\pi)_{\text{SOMO}}$, and $\text{NN}(n) \rightarrow \text{NN}(\pi)_{\text{SOMO}}$, where n represents in-plane MOs on NN and SQ. Prior spectral assignments have placed the $\text{SQ}(n) \rightarrow \text{SQ}(\pi)_{\text{SOMO}}$

transition in the $10,000\text{--}15,000\text{ cm}^{-1}$ region, and the $\text{NN}(n) \rightarrow \text{NN}(\pi)_{\text{SOMO}}$ transition in the $\sim 18,000\text{ cm}^{-1}$ region.^{22,36} We note that the low-energy transitions in **1** are noticeably broadened when compared to the corresponding bands in other $\text{Tp}^{\text{Cum,Me}}\text{M}(\text{SQ-NN})$ compounds.²² The intense transition at $22,870\text{ cm}^{-1}$ ($\epsilon \approx 8,000\text{ M}^{-1}\text{ cm}^{-1}$) is not present in the constituent SQ and NN chromophores²² and possesses an apparent high energy shoulder at $24,250\text{ cm}^{-1}$. We therefore assign this band as the $\text{SQ}(\pi)_{\text{SOMO}} \rightarrow \text{NN-Ph}(\pi^*-e_1)$ intraligand transition that possesses considerable $D \rightarrow A$ charge transfer character in accordance with previous assignments for **2** and **3**.²² The $\text{SQ}(\pi)_{\text{SOMO}} \rightarrow \text{NN-Ph}(\pi^*-e_1)$ charge transfer band in **1** is $\sim 1,700\text{ cm}^{-1}$ lower in energy than the corresponding $\text{SQ}(\pi)_{\text{SOMO}} \rightarrow \text{NN}(\pi^*)$ transition in **2**, which lacks the phenylene bridge. The lower energy of this transition in **1** can be understood in the context of Figure 2, where the strong $\text{NN}(\pi^*)\text{--Ph}(e_1)$ orbital mixing effectively lowers the energy of the $\text{NN}(\pi^*)\text{--Ph}(e_1)$ bonding MO relative to the $\text{SQ}(\pi)_{\text{SOMO}}$. An electron density difference map (EDDM) associated with the $\text{SQ}(\pi)_{\text{SOMO}} \rightarrow \text{NN-Ph}(\pi^*-e_1)$ transition is shown in Figure 4. The EDDM depicts the change in the

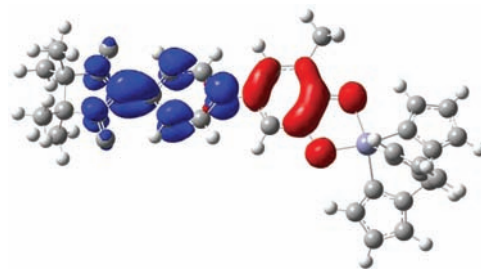


Figure 4. Calculated electron density difference map (EDDM) for the $\text{SQ}(\pi)_{\text{SOMO}} \rightarrow \text{NN-Ph}(\pi^*-e_1)$ $D \rightarrow A$ charge transfer band in **1** depicted at an isodensity value of 0.002 au . Red regions indicate a loss of electron density in the transition to the excited state, and blue regions indicate a gain of electron density in the transition to the excited state.

electron density of **1** that accompanies the $\text{SQ}(\pi)_{\text{SOMO}} \rightarrow \text{NN-Ph}(\pi^*-e_1)$ charge transfer excitation and clearly shows the dominant $D \rightarrow A$ nature of the intraligand $\text{SQ}(\pi) \rightarrow \text{NN-Ph}(\pi^*-e_1)$ transition and the importance of the phenylene bridge as part of the acceptor fragment. Finally, we assign the high energy transition at $26,800\text{ cm}^{-1}$ as a $\text{NN}\pi \rightarrow \pi^*$ transition on the basis of the spectral assignments for **2** and **3** and the presence of a similar band in Ar-NN.²²

Nature of the Bridge in the $D \rightarrow A$ Charge Transfer Excited State. Figures 2 and 4 indicate the importance of the phenylene bridge fragment in the $\text{SQ}(\pi)_{\text{SOMO}} \rightarrow \text{NN-Ph}(\pi^*-e_1)$ charge transfer transition. The importance of the phenylene bridge in mediating strong exchange coupling between the SQ and NN radical spins in **1** is also apparent in the magnitude of the ferromagnetic exchange interaction ($2J = +200\text{ cm}^{-1}$) determined from magnetic susceptibility experiments.³² Here we use a combination of resonance Raman spectroscopy, Raman excitation profiles, and hot band spectroscopy to gain greater insight into how the phenylene bridge contributes to the strong $D\text{--}B\text{--}A$ interaction and how the bridge distorts in the $\text{SQ}(\pi)_{\text{SOMO}} \rightarrow \text{NN-Ph}(\pi^*-e_1)$ charge transfer excited state. These spectroscopic studies are important for developing a greater understanding of bridge distortions that accompany molecular electron transfer/transport phenomena and contribute to the suppression of ballistic electron transport.

The solution resonance Raman spectra of **1** and **3** are shown in Figure 5 for comparative purposes. The data were collected

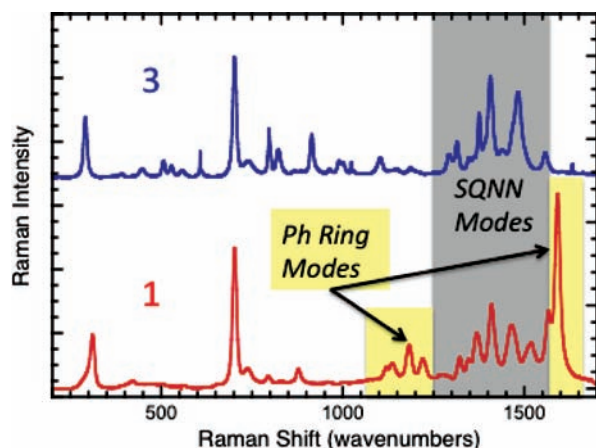


Figure 5. Room temperature resonance Raman spectra of $\text{Tp}^{\text{Cum,Me}}\text{Cu}(\text{SQ-NN})$ **3** (blue) and $\text{Tp}^{\text{Cum,Me}}\text{Zn}(\text{SQ-Ph-NN})$ **1** (red) at 413.7 nm. The solvent is CH_2Cl_2 .

using 413.7 nm excitation, which is in resonance with the $\text{SQ}(\pi)_{\text{SOMO}} \rightarrow \text{NN-Ph}(\pi^*-\text{e}_1)$ and $\text{SQ}(\pi)_{\text{SOMO}} \rightarrow \text{NN}(\pi^*)$ charge transfer bands of **1** and **3**, respectively. Vibrational bands in the 1,200–1,600 cm^{-1} region have previously been assigned as in-plane stretching vibrations associated with the SQ-NN ligand and were used to support the assignment of the $\text{SQ}(\pi)_{\text{SOMO}} \rightarrow \text{NN}(\pi^*)$ charge transfer band in **2** and **3**. The presence of highly coupled, in-plane SQ-NN modes for **1** is supported by the strong spectral similarity between **1** and **3** in the 1,200–1,600 cm^{-1} region of the spectrum. Compound **1** displays additional vibrations in the 1,100–1,250 cm^{-1} region of the spectrum and an intense Raman band at 1,591 cm^{-1} . The additional vibrational modes observed in **1** are anticipated to involve phenylene character due to their absence in the Raman spectra of **2** and **3**. The frequency of the 1,591 cm^{-1} vibration is very similar to the benzene e_{2g} vibration that occurs at $\sim 1,600 \text{ cm}^{-1}$ (Figure 6, top).

Vibrational frequency calculations performed on the SQ-Ph-NN ligand show modes at 1,664 and 1,618 cm^{-1} , both of which possess large displacements localized on the phenylene bridge that very closely resemble the 8a component of the doubly degenerate benzene e_{2g} vibration that is split in the low-symmetry environment of **1**. The 1,664 cm^{-1} mode can be described as an antisymmetric linear combination of the localized benzene 8a mode and an in-plane SQ mode (Ph(8a)-SQ), while the 1,618 cm^{-1} mode represents the symmetric, Ph(8a)+SQ combination (Figure 6, bottom).

A resonance Raman excitation profile has been constructed for the 1,591 cm^{-1} band in Figure 3, and the data show strong resonance enhancement of this vibration with excitation into the $\text{SQ}(\pi)_{\text{SOMO}} \rightarrow \text{NN-Ph}(\pi^*-\text{e}_1)$ charge transfer band. The strong resonance enhancement of the 1,591 cm^{-1} band directly results from a large excited state distortion along this vibrational coordinate. The origin of the strong resonance enhancement along the Ph(8a)-SQ(in-plane) coordinate can be understood in terms of the Kohn–Sham orbitals (Figure 7) that are associated with the dominant $\text{SQ}(\pi)_{\text{SOMO}} \rightarrow \text{NN-Ph}(\pi^*)$ one-electron promotion and the associated EDDM of Figure 4.

The transfer of $\text{SQ}(\pi)_{\text{SOMO}}$ electron density to the $\text{NN-Ph}(\pi^*)$ fragment in the charge transfer excited state results in a

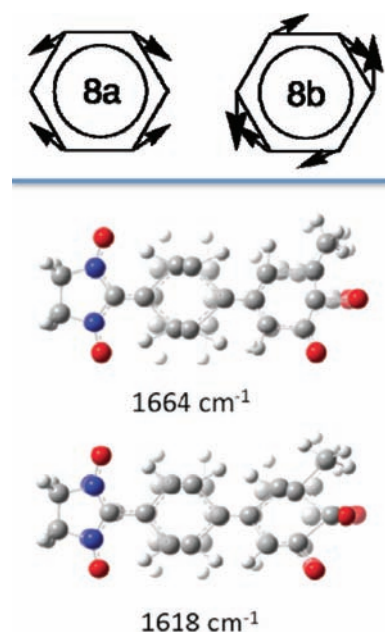


Figure 6. (Top) Representations of the e_{2g} vibrational modes of benzene. (Bottom) Representations of the two SQ-Ph-NN vibrational modes that possess contributions from the 8a (e_{2g}) benzene vibrational mode.

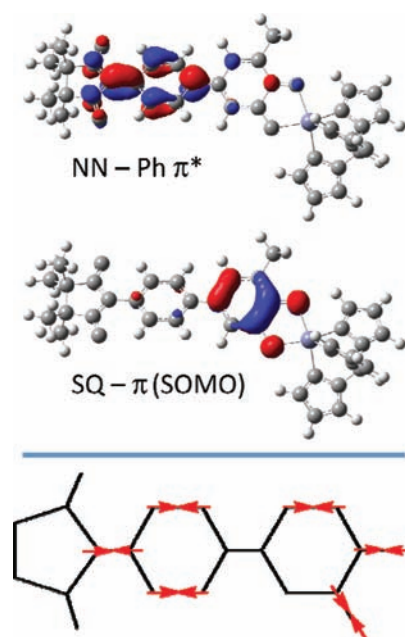


Figure 7. (Top) Principle Kohn–Sham orbitals of **1** that are involved in the $\text{SQ}(\pi)_{\text{SOMO}} \rightarrow \text{NN-Ph}(\pi^*)$ charge transfer (orbitals depicted at an isovalue of 0.05). (Bottom) Symmetrized excited state distortion coordinate derived from EDDM and Kohn–Sham orbitals associated with the $\text{SQ}(\pi)_{\text{SOMO}} \rightarrow \text{NN-Ph}(\pi^*-\text{e}_1)$ charge transfer transition in **1**.

phenylene bridge distortion along a mode that closely resembles the benzene 8a vibration. This bridge mode is enhanced via the Albrecht A-term mechanism³⁷ since this bridge mode transforms as a_1 in the localized D_{2h} phenylene symmetry present in the SQ-Ph-NN ligand. The phase of the SQ in-plane distortion relative to the phenylene 8a-type mode

is more difficult to ascertain, however. Inspection of orbital bonding and antibonding interactions in Figure 7 indicates that a depletion of $SQ(\pi)_{SOMO}$ electron density in the charge transfer excited state, coupled with population of the localized $NN-Ph(\pi^*)$ fragment, should result in a $SQ-Ph-NN$ excited state distortion along the symmetrized coordinate given in Figure 7 (bottom). In fact, the anticipated excited state distortion closely resembles the atom displacements present in the $1,618\text{ cm}^{-1}$ ground state vibrational mode. Thus, the primary excited state distortion that accompanies $SQ(\pi)_{SOMO} \rightarrow NN-Ph(\pi^*-e_1)$ charge transfer is along a vibrational coordinate best described as a symmetric $Ph(8a)+SQ(\text{in-plane})$ linear combination, and this underscores the dominant role of the phenylene bridge fragment acting as an electron acceptor in the D-B-A charge transfer excited state.

Additional evidence supporting an excited state distortion along the $Ph(8a)+SQ(\text{in-plane})$ symmetry coordinate derives from the variable temperature electronic absorption spectra of **1** given in Figure 8.

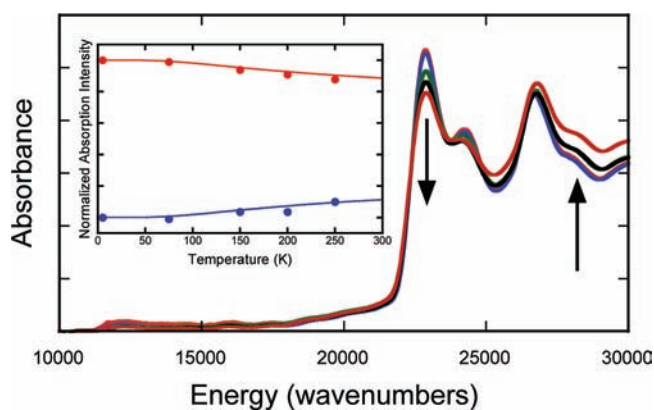


Figure 8. Variable temperature absorption spectra for **1** collected as a thin polymer film. Data collected at 5, 75, 150, 200, and 250 K. Inset: Normalized absorption intensity measured at $22,870\text{ cm}^{-1}$ (red circles) and at $28,200\text{ cm}^{-1}$ (blue circles). Red and blue lines are the Boltzmann populations of the 3GC and 1GC , respectively, determined by magnetic susceptibility measurements.

The ground state of **1** is a spin triplet ($S = 1$) with an exchange coupled singlet ($S = 0$) excited state residing 200 cm^{-1} higher in energy ($J = +100\text{ cm}^{-1}$).³² The inset of Figure 8 displays the same temperature dependence that is predicted from the Boltzmann population of the spin triplet (3GC) and spin singlet (1GC) ground configurations determined from variable-temperature magnetic susceptibility measurements.³² Therefore, both the $22,870\text{ cm}^{-1}$ $SQ(\pi)_{SOMO} \rightarrow NN-Ph(\pi^*-e_1)$ charge transfer band and its $24,250\text{ cm}^{-1}$ shoulder derive from the 3GC ground configuration. Thus, we suggest that the $24,250\text{ cm}^{-1}$ band is the $0 \rightarrow 1'$ vibronic transition built upon the $0 \rightarrow 0'$ origin at $22,870\text{ cm}^{-1}$, resulting in an excited state vibrational frequency of $1,380\text{ cm}^{-1}$. This excited state frequency represents an $\sim 13\%$ reduction when compared with the ground state $Ph(8a)+SQ(\text{in-plane})$ mode at $1,591\text{ cm}^{-1}$ that is strongly resonance enhanced in the Raman spectra of **1**. The observed frequency reduction of the $Ph(8a)+SQ(\text{in-plane})$ mode in the excited state is consistent with our spectral assignment and results from population of the $NN-Ph(\pi^*-e_1)$ orbital which possesses considerable antibonding character.

In summary, the results of bonding calculations, resonance Raman excitation profiles, and variable temperature electronic absorption spectroscopy point to a dominant excited state distortion along a $Ph(8a)+SQ(\text{in-plane})$ symmetry coordinate. Furthermore, the results underscore the importance of the $Ph(e_1)$ phenylene bridge orbital in facilitating $D \rightarrow A$ charge transfer in **1** and electron transport mediated by a 1,4-phenylene molecular wire placed between biased electrodes in a nanoscale device.

Determination of Intrinsic VBCI Parameters and Electronic Coupling Matrix Elements. Having developed a molecular orbital and vibronic description of how the phenylene bridge facilitates D-A coupling, we wish to further evaluate the nature of the D-A coupling by quantifying the magnitude of the electronic coupling matrix element (H_{ab}) in **1**. In order to accomplish this, we will use a valence bond configuration interaction (VBCI) approach. The VBCI model differs from the MO picture by virtue of the fact that it provides a state rather than an orbital description of the system. This is particularly relevant for spectroscopic studies since electronic transitions occur between states. In the VBCI model, D-A and D-B-A bond covalency results from configuration interaction between the ground configuration and excited configurations with H_{ab} being the off-diagonal matrix element that connects ground and excited state configurations of the same spin multiplicity. We previously used the ground state magnetic exchange coupling (J), the mean D-A charge transfer energy, U ($U = (E_{3EC} + E_{1EC})/2$), and an exchange integral (K_0) describing the $^3EC-^1EC$ splitting within a perturbative VBCI model to determine H_{ab} for **2** and **3** (Figure 9).²² Here, the

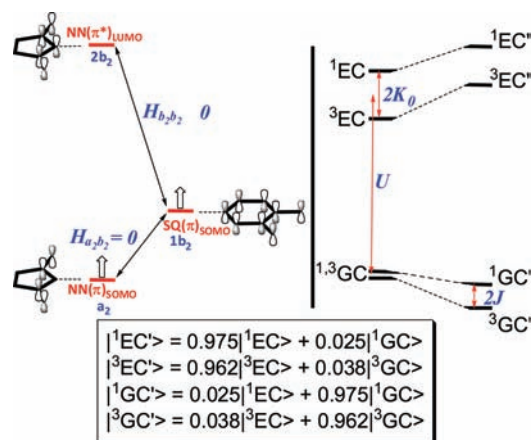


Figure 9. VBCI model. (Top) Simplified orbital diagram for **2** and **3** using $SQ(\pi)_{SOMO}$ ($1b_2$), $NN(\pi)_{SOMO}$ (a_2), and $NN(\pi^*)_{LUMO}$ ($2b_2$) basis functions (left), and a state diagram (right) deriving from $a_2^11b_2^1$ (1GC), $a_2^11b_2^1$ (3GC), $1b_2^12b_2^1$ (1EC), and $1b_2^12b_2^1$ (3EC) configurations. Primes indicate perturbed configurations. Note that a_2 and b_2 are local orbital symmetry labels, and the singlets are multideterminantal wave functions. (Bottom) VBCI wave functions derived from the 4×4 VBCI secular determinant (see text).

$^1,^3GC$ s are given by $a_2^11b_2^1$ and $a_2^11b_2^1$, and the $^1,^3EC$ s by $1b_2^12b_2^1$ and $1b_2^11b_2^1$. Due to the large magnitude of H_{ab} in these D-A biradicals, we use here a full-matrix diagonalization approach to determine the electronic coupling matrix element, H_{ab} , in nonbridged **3**. A combination of magnetic susceptibility and variable-temperature electronic absorption spectroscopy allowed us to determine the final state energies of 3GC , 1GC , 3EC , and 1EC for **3**.

These energies are simply the eigenvalues of the 4×4 VBCI Hamiltonian matrix given below.

	1GC	1EC	3GC	3EC
1GC	$0 - E$	H_{ab}	0	0
1EC	H_{ab}	$(U + K_0) - E$	0	0
3GC	0	0	$0 - E$	H_{ab}
3EC	0	0	H_{ab}	$(U - K_0) - E$

The simple VBCI matrix block diagonalizes into two 2×2 submatrices that yield four linear equations, allowing one to easily solve for H_{ab} , U , and K_0 analytically. The calculation yields $U = 19,885 \text{ cm}^{-1}$, $K_0 = 2,275 \text{ cm}^{-1}$, and $H_{ab} = 8,517 \text{ cm}^{-1}$, where the analytical value of H_{ab} for **3** compares with a value of $13,460 \text{ cm}^{-1}$ using the perturbative approach.²² The VBCI wave functions are given in Figure 9 (bottom). Using the expression

$$\frac{J_{\text{SQ-Ph-NN}}}{J_{\text{SQ-NN}}} = \frac{H_{\text{SQ-Ph-NN}}^2}{H_{\text{SQ-NN}}^2} \quad (1)$$

with $J_{\text{SQ-NN}} = 550 \text{ cm}^{-1}$ for **2**, and $J_{\text{SQ-Ph-NN}} = 100 \text{ cm}^{-1}$ and $H_{\text{SQ-NN}} = 8,517 \text{ cm}^{-1}$ for **2**, we obtain $H_{\text{SQ-Ph-NN}} = 3,632 \text{ cm}^{-1}$ for **1**.^{22,32} This represents a 57% decrease in H_{ab} when a phenylene bridges the SQ donor and NN acceptor. The large H_{ab} values that we have determined for these SQ-NN and SQ-Ph-NN biradicals result from their near coplanar structure and the strong π conjugation across the entire molecule.^{22,32}

Clearly, the largest magnitude of H_{ab} in any SQ-NN based donor–acceptor biradical occurs in nonbridged SQ-NN, where the SQ and NN fragments are hard wired directly to allow for maximal exchange between the SQ and NN fragments. The smallest H_{ab} value for these D-B-A systems is anticipated to occur when the D-A distance is infinitely long or when the SQ, bridge, and NN π systems are orthogonal to one another. However, it would be convenient if relationships could be developed that allow for an explicit correlation between H_{ab} and geometric structure without having to perform a detailed spectroscopic analysis. Recently, we showed that the magnitude of the isotropic N hyperfine interaction on the NN acceptor is a linear function of the NN nitrogen spin populations and that the isotropic N hyperfine is very sensitive to the nature and orientation of the bridge in SQ-bridge-NN donor–acceptor biradicals.³¹ We can therefore anticipate that an increase in D \rightarrow A charge transfer for these donor–acceptor biradicals should result in a corresponding increase in spin density on the acceptor fragment, and this can be conveniently monitored via the increase in magnitude of the NN nitrogen isotropic hyperfine coupling constant. In Figure 10 we correlate the experimentally determined H_{ab} for **1** and **2** with their respective experimentally determined NN nitrogen isotropic hyperfine coupling constants. The calculated isotropic N hyperfine coupling for a modified structure of **2**, where the SQ, phenyl, and NN rings are all mutually orthogonal, is presented in Figure 10 and serves as an analogue for a structure with $H_{ab} \approx 0$. An exponential rise function can be fit to these three data points to construct a calibration curve for the determination of H_{ab} for any SQ-bridge-NN system. An exponential rise function describing the magnitude of the D-A interaction is anticipated from simple orbital overlap considerations involving the exponential tail regions of the D and A wave functions. Furthermore, the beginning of the plateau region for an

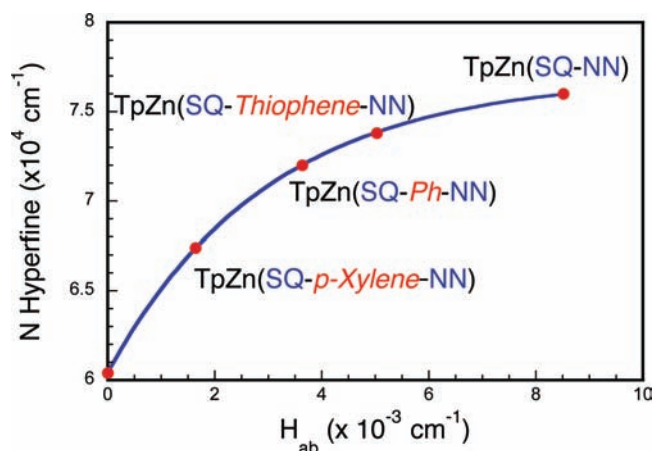


Figure 10. Plot of the experimentally determined isotropic N hyperfine on the NN acceptor fragment as a function of the electronic coupling matrix element for a series of SQ-bridge-NN systems. Blue line is the exponential rise function $6.04 + 1.65(1 - \exp(-0.33H_{ab}))$ ($R^2 = 0.999$).

exponential rise function will be well-defined by the H_{ab} value for $\text{Tp}^{\text{Cum,Me}}\text{Zn}(\text{SQ-NN})$, since H_{ab} for any D-B-A biradical should never exceed that of $\text{Tp}^{\text{Cum,Me}}\text{Zn}(\text{SQ-NN})$. The blue line in Figure 10 is the best fit of the exponential rise function to the N hyperfine versus H_{ab} data for $\text{Tp}^{\text{Cum,Me}}\text{Zn}(\text{SQ-bridge-NN})$ complexes using the biradical ligands SQ-NN and SQ-Ph-NN. However, we note that although the functional form for the A_{iso} versus H_{ab} data is well-described by an exponential rise function, there are intrinsic uncertainties that arise from the exponential fit to three data points. Nevertheless, all that is required to estimate H_{ab} for a given SQ-bridge-NN system is a determination of the NN nitrogen isotropic hyperfine parameter obtained from a simple analysis of the fluid solution EPR spectrum. We have determined the isotropic N hyperfine parameters for $\text{Tp}^{\text{Cum,Me}}\text{Zn}(\text{SQ-p-xylene-NN})$ and $\text{Tp}^{\text{Cum,Me}}\text{Zn}(\text{SQ-thiophene-NN})$,³¹ and these are also included in Figure 10 for comparative purposes. The H_{ab} value is significantly reduced (~45%) for nonplanar $\text{Tp}^{\text{Cum,Me}}\text{Zn}(\text{SQ-p-xylene-NN})$ from the corresponding value for $\text{Tp}^{\text{Cum,Me}}\text{Zn}(\text{SQ-Ph-NN})$ due to the loss of conjugation between the xylene, NN, and SQ π -systems.³¹ The loss of conjugation is due to the presence of the *p*-xylene methyl groups, which cause unfavorable steric interactions between the bridge and SQ and between the bridge and NN π systems and result in SQ-*p*-xylyl-NN torsional distortions.³¹ Additionally, we find that H_{ab} for $\text{Tp}^{\text{Cum,Me}}\text{Zn}(\text{SQ-thiophene-NN})$ is ~40% greater than that for $\text{Tp}^{\text{Cum,Me}}\text{Zn}(\text{SQ-Ph-NN})$. In summary, the results for $\text{Tp}^{\text{Cum,Me}}\text{Zn}(\text{SQ-thiophene-NN})$ and $\text{Tp}^{\text{Cum,Me}}\text{Zn}(\text{SQ-Ph-NN})$ are of interest for understanding long-range electronic coupling in polyphenylene and polythiophene intrinsically conducting polymers.

Relationship to Electron Transport using Molecular Wires. With respect to the large electronic coupling in **1** and **2**, it is of interest to note that very recently a molecular junction formed by a single benzene molecule bridging two biased Pt electrodes was shown to possess excellent electron transport properties with a conductance approaching the maximum allowed for conductance via a single channel, the quantum of conductance, G_0 .³⁰ In contrast to the 1,4-bridging geometry of benzene in **1**, where the charge transfer direction is along the C_2 axis of the bridge, the benzene molecular junction in the nanoelectrode system is suggested to bridge Pt contacts in a

cofacial manner whereby the C_6 axis of benzene is colinear with the charge transport direction. This leads to six channels for electron conductance using the 6 benzene p_z orbitals compared to a single channel available for π -type electron transfer/transport using a 1,4-phenylene linked system. Recently, van Ruitenbeek and co-workers used a combination of conductance measurements, isotope perturbations, and inelastic electron tunneling spectroscopy to probe the benzene distortion coordinate that is effectively coupled to charge transport.³⁰ They determined that that the distortion coordinate is described by a non-totally symmetric $\sim 400\text{ cm}^{-1}$ rotational mode about the C_6 axis of the benzene molecular junction.³⁰ In contrast, the distortion coordinate in **1** is along the totally symmetric 1,4-phenylene stretch, describing an effective electron transport/transfer channel as possessing quinoidal phenylene e_1 - π character. Our $H_{\text{SQ-Ph-NN}}$ value of $3,632\text{ cm}^{-1}$ for **1** strongly suggests high transmission coefficients are also possible in molecular junctions that utilize a 1,4-phenylene linkage with appropriate donor, bridge, an acceptor energy matching.

CONCLUSIONS

We have performed a detailed spectroscopic analysis on $\text{Tp}^{\text{Cum,Me}}\text{Zn}(\text{SQ-Ph-NN})$ **1**, which possesses a 1,4-phenylene linkage that bridges the SQ donor and NN acceptor, in order to develop greater insight into key bridge distortions that accompany electron transfer and electron transport in molecular and molecule-based systems. The intense charge transfer transition in **1** observed at $22,870\text{ cm}^{-1}$ has been assigned as a $\text{SQ}(\pi)_{\text{SOMO}} \rightarrow \text{NN-Ph}(\pi^*-e_1)$ intraligand transition that originates from the $S = 1$ ground state and possesses considerable $D \rightarrow A$ charge transfer character. A high energy shoulder is present at $24,250\text{ cm}^{-1}$ and is assigned as the $0 \rightarrow 1'$ vibronic transition that is built upon the $0 \rightarrow 0'$ origin at $22,870\text{ cm}^{-1}$, yielding an excited state vibrational frequency of $1,380\text{ cm}^{-1}$. We have assigned the $1,591\text{ cm}^{-1}$ $\text{Ph}(8a)+\text{SQ}$ - (in-plane) vibration as the 8a quinoidal type stretch in benzene, and the strong resonance enhancement of this vibration when exciting into the $\text{SQ}(\pi)_{\text{SOMO}} \rightarrow \text{NN-Ph}(\pi^*-e_1)$ $D \rightarrow A$ charge transfer band indicates there is a large excited state distortion along this vibrational coordinate. The excited state frequency is $\sim 13\%$ less than that observed for the $1,591\text{ cm}^{-1}$ $\text{Ph}(8a)+\text{SQ}$ - (in-plane) ground state mode that is strongly resonance enhanced in the Raman spectrum of **1**, consistent with our band assignment and the net antibonding character in the $\text{NN-Ph}(\pi^*-e_1)$ orbital. These data are consistent with the results of our bonding calculations that indicate a single phenylene bridge orbital (e_1) interacts very strongly with the NN acceptor fragment, but only weakly with the SQ donor fragment, and it is this strong $\text{NN}(\pi^*)\text{-Ph}(e_1)$ orbital interaction that effectively stabilizes the acceptor MO and lowers the intraligand CT transition in **1** relative to **2**. We have used a nonperturbative VBCI model to obtain spectroscopically derived electronic coupling matrix elements for **1** and **2**. The analysis yields $H_{\text{SQ-NN}} = 8,517\text{ cm}^{-1}$ for **2** and $H_{\text{SQ-Ph-NN}} = 3,632\text{ cm}^{-1}$ for **1**, indicating hard wiring a 1,4-phenylene linkage between the SQ donor and NN acceptor results in a 57% decrease in H_{ab} compared to the nonbridged SQ-NN dyad. Finally, we have developed a relationship between experimentally determined H_{ab} values and NN acceptor isotropic nitrogen hyperfine parameters so that the analysis of a simple isotropic EPR spectrum is all that is required to determine the magnitude of H_{ab} for any $\text{Tp}^{\text{Cum,Me}}\text{Zn}(\text{SQ-bridge-NN})$ D-B-A biradical system.

ASSOCIATED CONTENT

Supporting Information

Absolute energies (in Hartrees) and atomic coordinates for geometry optimizations. This material is available free of charge via the Internet at <http://pubs.acs.org>.

AUTHOR INFORMATION

Corresponding Author

mkirk@unm.edu; david_shultz@ncsu.edu

Notes

The authors declare no competing financial interest.

ACKNOWLEDGMENTS

M.L.K. acknowledges the National Institutes of Health (GM-057378) and the National Science Foundation (NSF CHE-1012928) for financial assistance. D.A.S. thanks the National Science Foundation (CHE-0910585) for financial support.

REFERENCES

- (1) Weiss, E. A.; Tauber, M. J.; Kelley, R. F.; Ahrens, M. J.; Ratner, M. A.; Wasielewski, M. R. *J. Am. Chem. Soc.* **2005**, *127*, 11842.
- (2) Barbara, P. F.; Meyer, T. J.; Ratner, M. A. *J. Phys. Chem.* **1996**, *100*, 13148.
- (3) Marcus, R. A. *Chem. Phys. Lett.* **1987**, *133*, 471.
- (4) Gray, H. B.; Walther, R. Ellis, J. In *Bioinorganic Chemistry*; Bertini, I., Gray, H. B., Lippard, S. J., Valentine, J. S., Eds.; University Science Books: Sausalito, CA, 1994; p 315.
- (5) Nakamoto, T.; Yoshida, M.; Kitagawa, S.; Katada, M.; Endo, K.; Sano, H. *Polyhedron* **1996**, *15*, 2131.
- (6) Wall, M. H.; Basu, P.; Buranda, T.; Wicks, B. S.; Findsen, E. W.; Ondrias, M.; Enemark, J. H.; Kirk, M. L. *Inorg. Chem.* **1997**, *36*, 5676.
- (7) Sekiguchi, S.; Kobori, Y.; Akiyama, K.; Tero-Kubota, S. *J. Am. Chem. Soc.* **1998**, *120*, 1325.
- (8) Bleuzen, A.; Lomenech, C.; Dolbecq, A.; Villain, F.; Goujon, A.; Roubeau, O.; Nogues, M.; Varret, F.; Baudelet, F.; Dartyge, E.; Giorgetti, C.; Gallet, J. J.; Moulin, C. C. D.; Verdaguier, M. *Mol. Cryst. Liq. Cryst. Sci. Technol., Sect. A* **1999**, *334*, 965.
- (9) Nelsen, S. F.; Ismagilov, R. F.; Gentile, K. E.; Powell, D. R. *J. Am. Chem. Soc.* **1999**, *121*, 7108.
- (10) Kuciauskas, D.; Liddell, P.; Lin, S.; Stone, S.; Moore, A.; Moore, T.; Gust, D. *J. Phys. Chem. B* **2000**, *104*, 4307.
- (11) Lewis, F.; Wu, T.; Liu, X.; Letsinger, R.; Greenfield, S.; Miller, S.; Wasielewski, M. *J. Am. Chem. Soc.* **2000**, *122*, 2889.
- (12) Miller, S.; Lukas, A.; Marsh, E.; Bushard, P.; Wasielewski, M. *J. Am. Chem. Soc.* **2000**, *122*, 7802.
- (13) Sato, O.; Hayami, S.; Gu, Z.; Seki, K.; Nakajima, R.; Fujishima, A. *Chem. Lett.* **2001**, 874.
- (14) Davis, W. B.; Ratner, M. A.; Wasielewski, M. R. *Chem. Phys.* **2002**, *281*, 333.
- (15) Tachikawa, T.; Kobori, Y.; Akiyama, K.; Katsuki, A.; Usui, Y.; Steiner, U. E.; Tero-Kubota, S. *Mol. Phys.* **2002**, *100*, 1413.
- (16) Lukas, A. S.; Bushard, P. J.; Weiss, E. A.; Wasielewski, M. R. *J. Am. Chem. Soc.* **2003**, *125*, 3921.
- (17) Goldsmith, R. H.; Sinks, L. E.; Kelley, R. F.; Betzen, L. J.; Liu, W. H.; Weiss, E. A.; Ratner, M. A.; Wasielewski, M. R. *Proc. Natl. Acad. Sci. U.S.A.* **2005**, *102*, 3540.
- (18) Weiss, E. A.; Tauber, M. J.; Ratner, M. A.; Wasielewski, M. R. *J. Am. Chem. Soc.* **2005**, *127*, 6052.
- (19) Weiss, E. A.; Wasielewski, M. R.; Ratner, M. A. *J. Chem. Phys.* **2005**, *123*, 064504.
- (20) Weiss, E. A.; Ahrens, M. J.; Sinks, L. E.; Gusev, A. V.; Ratner, M. A.; Wasielewski, M. R. *J. Am. Chem. Soc.* **2004**, *126*, 5577.
- (21) Sinks, L. E.; Weiss, E. A.; Giaimo, J. M.; Wasielewski, M. R. *Chem. Phys. Lett.* **2005**, *404*, 244.
- (22) Kirk, M. L.; Shultz, D. A.; Depperman, E. C.; Brannen, C. L. *J. Am. Chem. Soc.* **2007**, *129*, 1937.

- (23) Ke, S. H.; Baranger, H. U.; Yang, W. T. *Phys. Rev. B* **2005**, *71*, 113401.
- (24) Liu, R.; Ke, S. H.; Baranger, H. U.; Yang, W. T. *J. Chem. Phys.* **2005**, *122*, 044703.
- (25) Metzger, R. *Mater. Sci. Eng.* **1995**, *C3*, 277.
- (26) Stokbro, K.; Taylor, J.; Brandbyge, M. *J. Am. Chem. Soc.* **2003**, *125*, 3674.
- (27) Metzger, R. M.; Chen, B.; Hopfner, U.; Lakshmikantham, M. V.; Vuillaume, D.; Kawai, T.; Wu, X. L.; Tachibana, H.; Hughes, T. V.; Sakurai, H.; Baldwin, J. W.; Hosch, C.; Cava, M. P.; Brehmer, L.; Ashwell, G. J. *J. Am. Chem. Soc.* **1997**, *119*, 10455.
- (28) Aviram, A.; Ratner, M. A. *Chem. Phys. Lett.* **1974**, *29*, 277.
- (29) Venkataraman, L. *Physics* **2008**, *1*.
- (30) Kiguchi, M.; Tal, O.; Wohlthat, S.; Pauly, F.; Krieger, M.; Djukic, D.; Cuevas, J. C.; van Ruitenbeek, J. M. *Phys. Rev. Lett.* **2008**, *101*, 046801.
- (31) Kirk, M. L.; Shultz, D. A.; Habel-Rodriguez, D.; Schmidt, R. D.; Sullivan, U. *J. Phys. Chem. B* **2010**, *114*, 14712.
- (32) Shultz, D. A.; Vostrikova, K. E.; Bodnar, S. H.; Koo, H. J.; Whangbo, M. H.; Kirk, M. L.; Depperman, E. C.; Kampf, J. W. *J. Am. Chem. Soc.* **2003**, *125*, 1607.
- (33) Shultz, D. A.; Bodnar, S. H. *Inorg. Chem.* **1999**, *38*, 591.
- (34) Frisch, M. J.; G. W. T., Schlegel, H. B.; Scuseria, G. E.; Robb, M. A.; Cheeseman, J. R.; Montgomery, J. A., Jr., Vreven, T.; Kudin, K. N.; Burant, J. C.; Millam, J. M.; Iyengar, S. S.; Tomasi, J.; Barone, V.; Mennucci, B.; Cossi, M.; Scalmani, G.; Rega, N.; Petersson, G. A.; Nakatsuji, H.; Hada, M.; Ehara, M.; Toyota, K.; Fukuda, R.; Hasegawa, J.; Ishida, M.; Nakajima, T.; Honda, Y.; Kitao, O.; Nakai, H.; Klene, M.; Li, X.; Knox, J. E.; Hratchian, H. P.; Cross, J. B.; Bakken, V.; Adamo, C.; Jaramillo, J.; Gomperts, R.; Stratmann, R. E.; Yazyev, O.; Austin, A. J.; Cammi, R.; Pomelli, C.; Ochterski, J. W.; Ayala, P. Y.; Morokuma, K.; Voth, G. A.; Salvador, P.; Dannenberg, J. J.; Zakrzewski, V. G.; Dapprich, S.; Daniels, A. D.; Strain, M. C.; Farkas, O.; Malick, D. K.; Rabuck, A. D.; Raghavachari, K.; Foresman, J. B.; Ortiz, J. V.; Cui, Q.; Baboul, A. G.; Clifford, S.; Cioslowski, J.; Stefanov, B. B.; Liu, G.; Liashenko, A.; Piskorz, P.; Komaromi, I.; Martin, R. L.; Fox, D. J.; Keith, T.; M. A. Al-Laham, Peng, C. Y.; Nanayakkara, A.; Challacombe, M.; Gill, P. M. W.; Johnson, B.; Chen, W.; Wong, M. W.; Gonzalez, C.; Pople, J. A. *Gaussian 03W*; Gaussian, Inc.: Wallingford, CT, 2004.
- (35) O'Boyle, N. M.; Tenderholt, A. L.; Langner, K. M. *J. Comput. Chem.* **2008**, *29*, 839.
- (36) Kirk, M. L.; Shultz, D. A.; Depperman, E. C. *Polyhedron* **2005**, *24*, 2880.
- (37) Albrecht, A. C. *J. Chem. Phys.* **1961**, *34*, 1476.